Sensors and Actuators A 312 (2020) 112092

Contents lists available at ScienceDirect

Sensors and Actuators A: Physical

journal homepage: www.elsevier.com/locate/sna

Amplitude noise spectrum of a lock-in amplifier: Application to microcantilever noise measurements

Michael G. Ruppert*, Nathan J. Bartlett, Yuen K. Yong, Andrew J. Fleming

University of Newcastle, Callaghan, NSW 2308, Australia

ARTICLE INFO

Article history:
Received 8 January 2020
Received in revised form 5 May 2020
Accepted 20 May 2020
Available online 29 May 2020

Keywords:
Lock-in amplifier
Demodulation
Atomic force microscopy
Estimation
Noise spectral density
Thermal noise

ABSTRACT

The lock-in amplifier is a crucial component in many applications requiring high-resolution displacement sensing; it's purpose is to estimate the amplitude and phase of a periodic signal, potentially corrupted by noise, at a frequency determined by a reference signal. Where the noise can be approximated by a stationary Gaussian process, such as thermal force noise and electronic sensor noise, this article derives the amplitude noise spectral density of the lock-in-amplifier output. The proposed method is demonstrated by predicting the demodulated noise spectrum of a microcantilever for dynamic-mode atomic force microscopy to determine the cantilever on-resonance thermal noise, the cantilever tracking bandwidth and the electronic noise floor. The estimates are shown to closely match experimental results over a wide range of operating conditions.

1. Introduction

The principle of modulation is used in many high resolution sensor applications [1] such as linear position sensors [2], capacitive sensors [3], and inductive sensors [4] to increase the signal-to-noise ratio of weak signals buried in noise. One of the most celebrated applications of sensing using modulation are dynamic imaging modes [5] in atomic force microscopy (AFM) [6]. In these modes, a microcantilever is excited at one of its resonance frequencies while a sample is scanned underneath the sharp oscillating cantilever tip. As a result of surface properties of the sample, the amplitude and phase of the cantilever oscillation signal are modulated by the non-linear tip-sample interaction force. By employing a feedback loop to maintain a fixed cantilever oscillation amplitude or phase shift, high-resolution 3D images of the sample topography [7] and material properties [8] can be obtained.

At the heart of dynamic AFM imaging methods, a demodulator is employed to determine the amplitude and phase of the cantilever deflection signal. A number of demodulation techniques for high-speed AFM [9–12] and multifrequency AFM [13–15] can be found in the literature, some of which have found regular use in commercial AFM systems. Demodulation methods can be classified as non-synchronous (using rectification) and synchronous (using multiplication with a reference oscillator) [16]. While rectification methods can be simple to implement and can achieve very high tracking bandwidths, they are unable to recover phase information and are outperformed by synchronous methods in terms of their noise performance [16]. In contrast, the lock-in amplifier (LIA) [17–19] is a narrow-band technique which is insensitive to other frequency components. Due to its is unparalleled noise performance, the lock-in amplifier has been adopted as the industry wide standard in commercial AFMs [16] but is also widely used for electrochemical [20] and low-frequency noise measurements [21].

This article derives the amplitude noise spectral density of a lock-in amplifier, which is then applied to predict the amplitude noise spectrum a microcantilever for dynamic-mode AFM as shown in Fig. 1. For this purpose, the effect of the cantilever thermal noise and electronic sensor noise on the amplitude estimate are studied with simulations and with experiments. A single measurement of the amplitude noise spectral density can be used to predict (1) the on-resonance thermal noise of the cantilever, (2) the cantilever tracking bandwidth, and (3) the electronic noise floor if the cantilever parameters and deflection sensitivity are known. The approach has several benefits compared to conventional means to obtain these values. First, the approach reduces computational burden on the digital signal processing system. For instance, recording the thermal noise response of a high-frequency cantilever can pose a significant challenge since the sample frequency and sample time need to be sufficiently large to measure the response accurately. Second, the cantilever tracking bandwidth can be measured non-

* Corresponding author.
E-mail address: michael.ruppert@newcastle.edu.au (M.G. Ruppert).

https://doi.org/10.1016/j.sna.2020.112092
0924-4247/

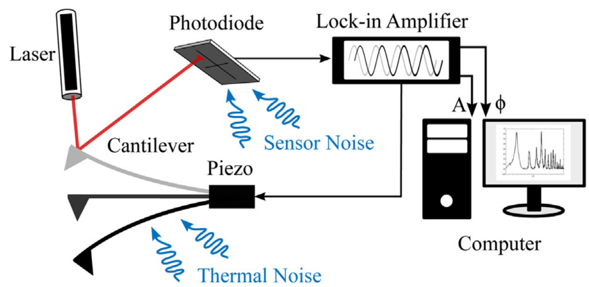

Fig. 1. Schematic of an AFM cantilever noise measurement. The cantilever is actively driven at resonance while being subject to thermal noise and electronic noise from an optical beam deflection sensor. The oscillation amplitude is demodulated using a lock-in amplifier.

invasively without having to bring the cantilever in contact with the sample. This provides *a priori* information to optimize the lock-in amplifier low-pass filter bandwidth and z-axis controller gain.

2. Principle of lock-in demodulation

The principle of demodulating a sinusoidal signal with known angular carrier frequency ω_0 and unknown amplitude A and phase ϕ of the form

$$y(t) = A\sin(\omega_0 t + \phi) \tag{1}$$

is depicted in Fig. 2. In the inset, an amplitude modulated signal is shown, where the modulation process creates distinct frequency components located at f_0 and $f_0 \pm f_m$ (upper and lower sidebands centered symmetrically around the carrier frequency). The lock-in amplifier implementation, graphically depicted in Fig. 2, includes a multiplication of the input signal (1) with in-phase and quadrature sinusoids to obtain

$$\begin{aligned} y_{\mathrm{i}} = y\sin(\omega_0 t) &= \frac{1}{2}A\left[\cos(\phi) - \cos(2\omega_0 t + \phi)\right] \\ &= \frac{1}{2}x_i - \frac{1}{2}A\cos(2\omega_0 t + \phi) \end{aligned} \tag{2}$$

and

$$\begin{aligned} y_{\mathrm{q}} = y\cos(\omega_0 t) &= \frac{1}{2}A\left[\sin(\phi) + \sin(2\omega_0 t + \phi)\right] \\ &= \frac{1}{2}x_q + \frac{1}{2}A\cos(2\omega_0 t + \phi) \end{aligned} \tag{3}$$

with the in-phase and quadrature states

$$x_i = A\cos\phi, \quad x_q = A\sin\phi. \tag{4}$$

It can be seen that the multiplication generates harmonics at $2\omega_0$, which are removed by employing a low-pass filter $F(s)$ with cut-off frequency much lower than $2\omega_0$. Naturally, the order and cut-off frequency of the low-pass filter determines the bandwidth and noise of the amplitude estimate. At the output of the lock-in amplifier the amplitude is then obtained by the non-linear calculation

$$A = 2\sqrt{\left(\frac{1}{2}x_i\right)^2 + \left(\frac{1}{2}x_q\right)^2}. \tag{5}$$

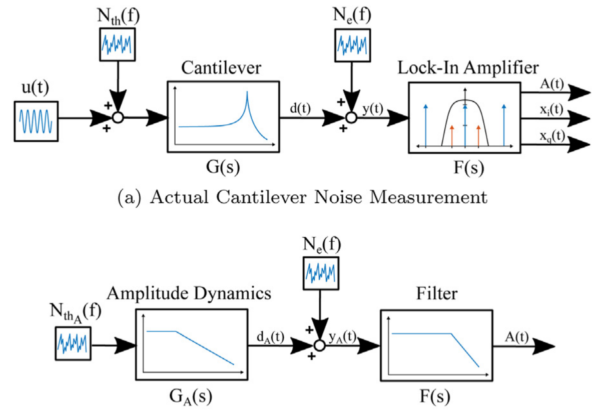

(a) Actual Cantilever Noise Measurement

(b) Linearized Cantilever Noise Measurement

Fig. 3. Block diagrams of the actual and linearized noise measurement setups. (a) Block diagram of the nonlinear signal flow with second-order cantilever model and lock-in amplifier. (b) Equivalent linear block diagram of the signal flow with first-order amplitude dynamics and low-pass filter.

3. Analysis of cantilever noise spectral density

In this section, a cantilever noise measurement is analyzed and the nonlinear signal flow in the lock-in amplifier is compared to an equivalent linear model to predict the noise spectral density of the quadrature and in-phase components and estimated amplitude. The actual measurement setup is shown in Fig. 3(a). Here, a cantilever, represented by a second-order transfer function model, is subjected to an active driving force u(t) as well as to a white thermal force noise with a noise spectral density $N_{\mathrm{th}}(f)$. The resulting deflection d is measured with an optical beam deflection sensor [22] which adds white sensor noise with a noise spectral density of $N_e(f)$. The resulting signal y is passed through a lock-in amplifier as depicted in Fig. 2 containing a demodulation low-pass filter $F(s)$ with cut-off frequency f_{LIA} to measure the cantilever vibrational amplitude.

In order to predict the noise spectral density in the amplitude, the linear block diagram in Fig. 3(b) is proposed. Here, a first-order model for the amplitude dynamics is suggested and the equivalent white thermal amplitude noise $w_{\mathrm{A}}(t)$ with a noise spectral density $N_{\mathrm{th_A}}(f)$ is derived such that the total integrated noise is preserved. The resulting displacement is subjected to the same white sensor noise and is passed directly through the demodulation low-pass

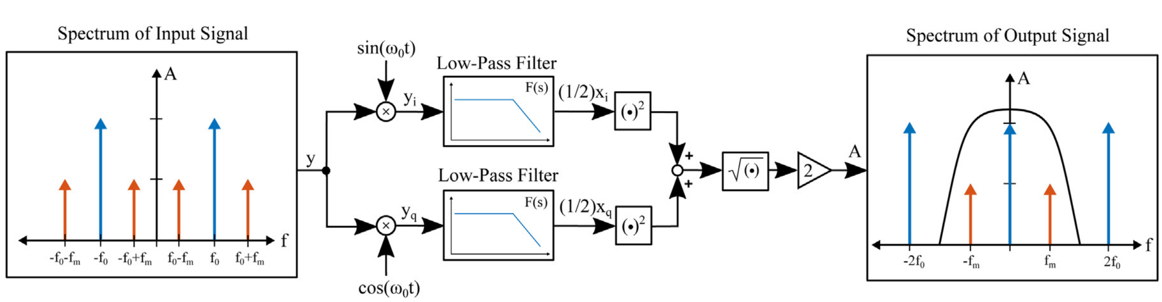

Fig. 2. Functional block diagram of a lock-in amplifier implementation. An amplitude modulated signal with distinct frequency components located at f_0 and $f_0 \pm f_m$ is passed through the nonlinear signal chain and filtered to obtain an amplitude estimate of the input signal. The order and cut-off frequency of the low-pass filter directly determines the tracking bandwidth and noise in the amplitude estimate.

filter $F(s)$. In the following subsections, the noise spectral densities of each signal are derived individually.

3.1. Cantilever model

A single mode of the cantilever can be approximated by a second order differential equation of the form

$$\ddot{d}(t) + \frac{\omega_0}{Q}\dot{d}(t) + \omega_0^2 d(t) = \frac{\omega_0^2}{k}u(t) \tag{6}$$

where $u(t)$ is an input force, $d(t)$ is the deflection at the tip, Q is the quality factor and ω_0 is the resonance frequency. The eigenvalues of (6) for $u(t) \equiv 0$ are given by

$$\lambda_{1,2} = -\frac{\omega_0}{2Q} \pm j\omega_0\sqrt{1 - \frac{1}{4Q^2}} \tag{7}$$

and hence the real-part of the eigenvalues characterize the cantilever amplitude tracking bandwidth as

$$f_c = \frac{f_0}{2Q}. \tag{8}$$

For a standard intermittent contact-mode cantilever such as the TAP190-G (Budget Sensors) with a resonance frequency of $f_0 = 190$ kHz and a natural Q factor of $Q = 400$, the tracking bandwidth is approximately $f_c = 237.5$ Hz. In intermittent contact-mode AFM, the cantilever is actively driven at resonance with $u(t) = F_d \sin\omega_0 t$ where F_d is the driving force amplitude. Then, the transfer function from input force to tip deflection is given as

$$G(s) = \frac{\alpha\omega_0^2}{s^2 + \frac{\omega_0}{Q}s + \omega_0^2} \tag{9}$$

and has units of [m/N] where $\alpha = 1/k$ is the DC-gain of the system. The magnitude of the cantilever transfer function is given by

$$|G(j2\pi f)| = \sqrt{\frac{1/k^2}{\left(1 - \frac{f^2}{f_0^2}\right)^2 + \frac{f^2}{f_0^2 Q^2}}}. \tag{10}$$

Evaluating (10) at $f = f_0$ and assuming a driving force amplitude of F_d, the expected amplitude A_d of the cantilever displacement $d(t)$ is given by

$$A_d = |G(j2\pi f_0)|F_d = \frac{QF_d}{k}. \tag{11}$$

Note that in the absence of thermal and measurement noise, $A = A_d$ in (1).

3.2. Cantilever thermal noise

The equipartition theorem states that if a system is in thermal equilibrium, the total energy of each vibrational mode has a mean value equal to $1/2k_BT$, where k_B is the Boltzman constant and T is the absolute temperature [23]. If an optical beam deflection sensor is used to measure the fundamental mode cantilever deflections, a correction factor has to be applied and the variance of the cantilever thermal noise vibrations σ_d^2 [m^2] is given by [24]

$$\sigma_d^2 = 0.8175\frac{k_BT}{k}. \tag{12}$$

The correction factor takes into account the effect of higher order modes (the cantilever is not a perfect simple harmonic oscillator) and the fact that the optical beam deflection sensor measures inclination rather than true displacement.

The variance of the cantilever deflections and the deflection noise spectral density N_d [m/$\sqrt{\text{Hz}}$] are related by

$$\sigma_d^2 = \int_0^\infty N_d^2(f)df = \int_0^\infty N_{\text{th}}^2(f)|G(j2\pi f)|^2 df \tag{13}$$

where $N_{\text{th}}(f)$ is the white thermal force noise [N/$\sqrt{\text{Hz}}$]. Substituting (10) into (13), yields

$$\sigma_d^2 = \frac{N_{\text{th}}^2}{k^2}\int_0^\infty \frac{1}{\left(1 - \frac{f^2}{f_0^2}\right)^2 + \frac{f^2}{f_0^2Q^2}}df \tag{14}$$

$$= \frac{N_{\text{th}}^2}{k^2}\int_0^\infty \frac{1}{\left(\frac{f}{f_0}\right)^4 + \left(\frac{1}{Q^2} - 2\right)\left(\frac{f}{f_0}\right)^2 + 1}df. \tag{15}$$

The integral can be solved using the substitution $x = \frac{f}{f_0}$ and the following integral pair [25]

$$\int_0^\infty \frac{1}{x^4 + bx^2 + c}dx = \frac{\pi}{2}\frac{1}{\sqrt{b + 2\sqrt{c}}} \tag{16}$$

which yields

$$\sigma_d^2 = \frac{N_{\text{th}}^2}{k^2}\frac{\pi}{2}f_0Q. \tag{17}$$

Using (12), the white thermal force noise drive is found to be

$$N_{\text{th}}(f) = \sqrt{0.8175\frac{2kk_BT}{\pi f_0 Q}} \tag{18}$$

and the thermal deflection noise spectral density is obtained as

$$N_d(f) = \sqrt{0.8175\frac{2kk_BT}{\pi f_0 Q}}\sqrt{\frac{\frac{1}{k^2}}{\left(1 - \frac{f^2}{f_0^2}\right)^2 + \frac{f^2}{f_0^2Q^2}}}. \tag{19}$$

Evaluating (19) at $f = f_0$ yields the thermal deflections at resonance

$$N_d(f_0) = \sqrt{0.8175\frac{2k_BTQ}{k\pi f_0}}. \tag{20}$$

A simulation of the thermal noise spectral density $N_d(f)$ of a cantilever with a resonance frequency of $f_0 = 190$ kHz and first mode stiffness of $k = 48$ N/m for varying Q factors is shown in Fig. 4(a) along with the theoretical thermal noise spectral density (19). Due to the dependence of (18),(19), and (20) on the cantilever Q factor, low-frequency thermal noise is decreased and on-resonance thermal noise is increased as the Q factor increases. However, as predicted by the equipartition theorem (12) and (13), the integrated noise is constant which can be seen in the inset in Fig. 4(a). For high Q factors, most of the energy is contained in the sharp resonance which causes a numerical artifact in the total integrated noise. This can be counteracted by increasing the frequency resolution.

3.3. Measurement noise

Traditionally, the optical beam deflection (OBD) method [22] is used in intermittent contact-mode AFM to measure the cantilever vibrations. OBD sensor noise consists of laser and photodiode shot noise as well as electronic noise of the read-out circuit [26–28]. Assuming a well-designed OBD system, the photodiode shot noise is usually dominant and sets the lower limit for the deflection noise [26,27]. Scaled to distance units by the deflection sensitivity of the read-out, commercial OBD systems achieve a white noise spectral density in the range of $N_e(f) = 100 - 1000$ fm/$\sqrt{\text{Hz}}$ [26].

Adding bandwidth-limited white measurement noise with $N_e(f) = 100$ fm/$\sqrt{\text{Hz}}$ to the simulations shown in Fig. 4(a) leads to

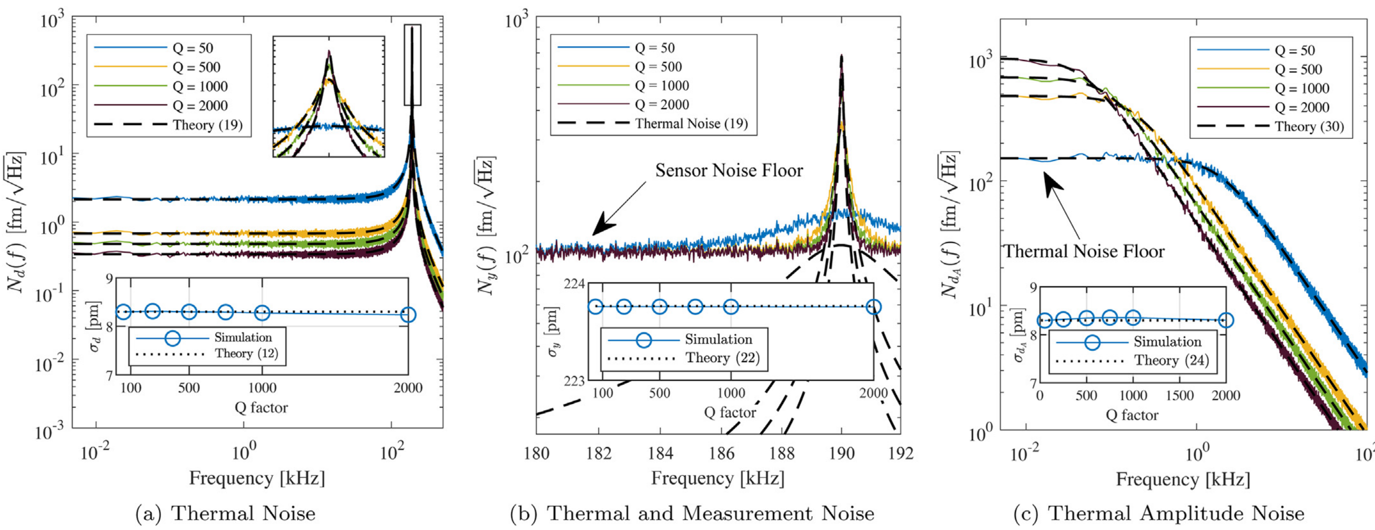

Fig. 4. Simulation of cantilever noise processes. (a) Thermal deflection noise spectral density $N_d(f)$ of a tapping-mode AFM cantilever for varying cantilever Q factors. (b) Total noise spectral density $N_y(f)$ of a tapping-mode AFM cantilever for varying Q factors. (c) Thermal amplitude noise spectral density $N_{d_A}(f)$ for varying cantilever Q factors. The insets show the respective total integrated noise as a function of cantilever Q factor. Simulation parameters: $f_0 = 190$ kHz, $k = 48$ N/m, $N_e(f) = 100\,\mathrm{fm}/\sqrt{\mathrm{Hz}}$.

the spectra shown in Fig. 4(b). The additional sensor noise has the effect of shifting the spectrum according to

$$N_y(f) = \sqrt{N_e(f)^2 + N_d(f)^2}. \tag{21}$$

Since the high Q cantilever focuses most of the thermal noise in the resonance, this shift is hardly observed at the resonance. In contrast, the thermal noise of the low Q cantilever is spread out (compare low-frequency noise floor in Fig. 4(a)) which leads to a substantial difference between the total noise density and (19). For the high Q cantilever simulations, the white noise floor away from the resonance is easily observed to be at the measurement noise value of $N_e(f) = 100\,\mathrm{fm}/\sqrt{\mathrm{Hz}}$. The variance of the cantilever deflections due to thermal and measurement noise is calculated as

$$\sigma_y^2 = \int_0^\infty N_y^2(f)df \tag{22}$$

Comparing the insets of Fig. 4(a) and (b), the total integrated noise is dominated by the measurement noise.

3.4. Equivalent model for amplitude noise

In intermittent contact-mode AFM, the noise in the amplitude of the cantilever oscillation determines the minimal resolution in the topography image. Assuming the cantilever is in constant excitation, the amplitude dynamics are given by the first-order approximation

$$G_A(s) = \frac{\beta \frac{\omega_0}{2Q}}{s + \frac{\omega_0}{2Q}}. \tag{23}$$

The first order amplitude dynamics is a low-pass filter with cut-off frequency of $f_c = \frac{f_0}{2Q}$ and $\beta = 1$ nm/nm is the amplitude sensitivity for medium to stiff samples and relatively high Q factors and states the theoretical upper limit [29,30]. In order to maintain the thermal noise spectrum in the amplitude of the cantilever, the following equation must hold

$$\sigma_{d_A}^2 = \int_0^\infty N_{\mathrm{th}_A}^2 |G_A(j2\pi f)|^2 df \overset{\mathrm{def}}{=} 0.8175\frac{k_B T}{k} \tag{24}$$

where N_{th_A} is the spectral density of the equivalent thermal noise input and

$$|G_A(j2\pi f)|^2 = \frac{f_c^2}{f_c^2 + f^2} \tag{25}$$

is the magnitude of the amplitude transfer function of the cantilever. Substituting (25) into (24) yields

$$\sigma_{d_A}^2 = N_{\mathrm{th}_A}^2 \int_0^\infty \frac{f_c^2}{f_c^2 + f^2} df \tag{26}$$

which can be solved using the following integral pair [25]

$$\int \frac{1}{a^2 + x^2} dx = \frac{1}{a}\tan^{-1}\left(\frac{x}{a}\right) \tag{27}$$

which leads to

$$\sigma_{d_A}^2 = N_{\mathrm{th}_A}^2 f_c^2 \left[\frac{1}{f_c}\tan^{-1}\left(\frac{f}{f_c}\right)\right]_0^\infty = N_{\mathrm{th}_A}^2 f_c \frac{\pi}{2}. \tag{28}$$

Solving the above equation for N_{th_A} and using (24) yields

$$N_{\mathrm{th}_A} = \sqrt{0.8175\frac{4k_B T Q}{k f_0 \pi}} = \sqrt{2} N_d(f_0). \tag{29}$$

Hence, the thermal amplitude noise spectral density is given by

$$N_{d_A}(f) = \sqrt{2} N_d(f_0) |G_A(j2\pi f)|. \tag{30}$$

A simulation is shown in Fig. 4(c). For increasing Q factors, the increase in thermal deflection noise at the resonance is replicated by an increased noise floor at low frequencies. Also clearly visible is the increase in cantilever tracking bandwidth as the Q factor is decreased. However, as the integral (24) must hold, the RMS noise is constant irrespective of the cantilever Q factor as can be seen in the inset in Fig. 4(c).

3.5. In-phase and quadrature noise densities

If a lock-in amplifier is used for cantilever noise measurements, the multiplication operations, low-pass filtering with $F(s)$, summation, and the non-linearities in the signal chain (Fig. 2) need to be taken into account to determine the noise spectral density of the amplitude estimate. The noise spectral density of the in-phase and

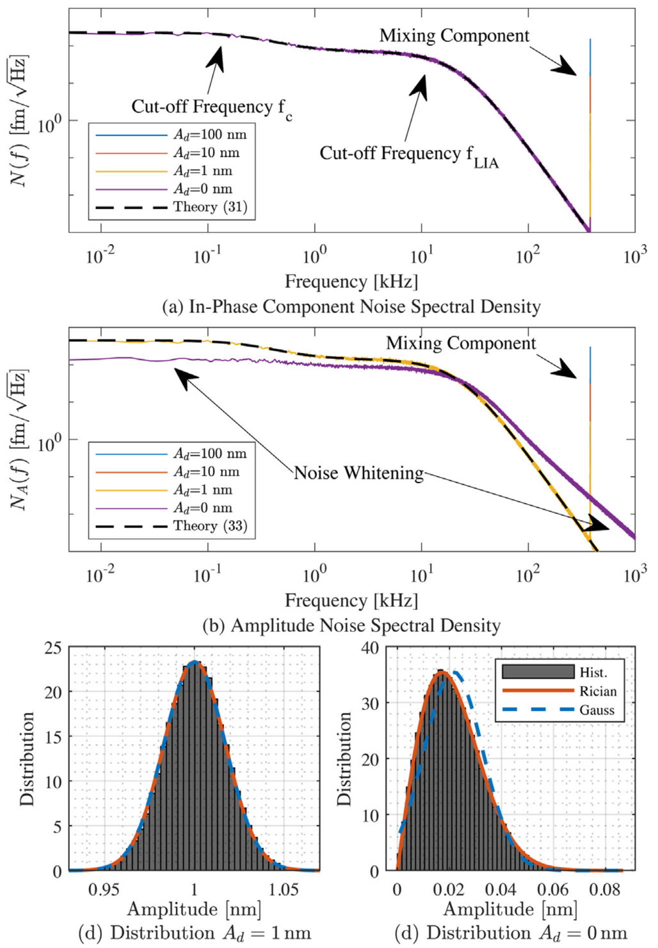

Fig. 5. Simulation of the in-phase and amplitude noise density estimates and probability density functions. (a) Noise spectral density of the in-phase component $1/2x_i$. (b) Noise spectral density of the amplitude A. Histogram and probability density function of the amplitude for (c) $A_d = 1$ nm and (d) $A_d = 0$ nm. Simulation parameters: $f_0 = 190$ kHz, $k = 48$ N/m, $Q = 400$, $N_e(f) = 100\,\text{fm}/\sqrt{\text{Hz}}$, $f_{\text{LIA}} = 10$ kHz.

quadrature component are equal (compare A) and can be calculated as $N_{\frac{1}{2}x_i}(f) = N_{\frac{1}{2}x_q}(f) = N(f)$ where

$$N(f) = \sqrt{\left(\frac{\sqrt{2}}{2}\right)^2 N_{e,F}^2(f) + \left(\frac{\sqrt{2}}{2}\right)^2 N_{d_A,F}^2(f)} \tag{31}$$

and

$$\begin{aligned} N_{e,F}(f) &= N_e(f)|F(j2\pi f)| \\ N_{d_A,F}(f) &= N_d(f_0)|G_A(j2\pi f)||F(j2\pi f)| \end{aligned} \tag{32}$$

The simulated noise density function of the in-phase component and the linear approximation (31) are shown in Fig. 5(a) for varying cantilever driving amplitudes. It can be seen that the noise estimate is independent of the cantilever drive and accurately follows the linear model even in the absence of an active driving force. A mixing component at $2f_0$ is visible whose magnitude depends on the drive amplitude. The noise spectral density is characterized by the cantilever amplitude dynamics $G_A(s)$ with cut-off frequency f_c and the demodulation low-pass filter $F(s)$ with cut-off frequency f_{LIA}, as highlighted in Fig. 5(a).

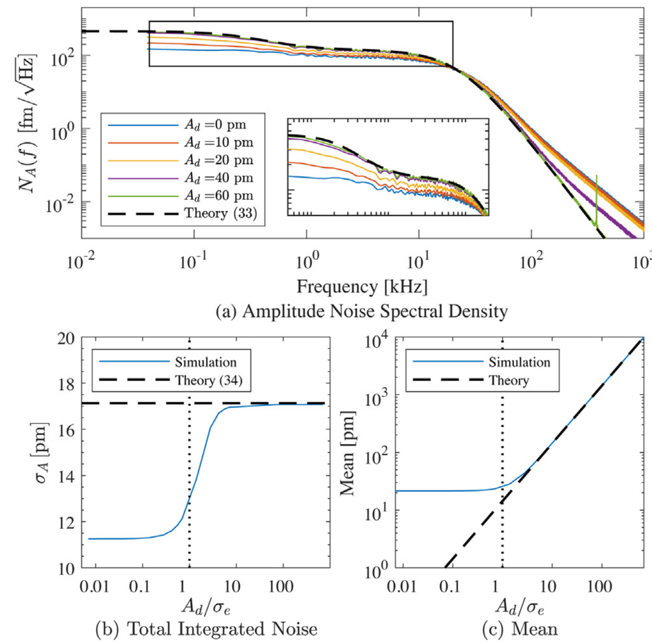

Fig. 6. Simulation of the amplitude noise spectral density for different amplitudes. (a) Amplitude noise spectral density, (b) total integrated noise as a function of the ratio A_d/σ_e, and (c) mean as a function of the ratio A_d/σ_e, *Theory* indicates the correct amplitude. The vertical dotted line marks the ratio of $A_d/\sigma_e = 1$. Simulation parameters: $f_0 = 190$ kHz, $k = 48$ N/m, $Q = 400$, $N_e(f) = 100\,\text{fm}/\sqrt{\text{Hz}}$, $f_{\text{LIA}} = 10$ kHz.

3.6. *Amplitude noise density*

The amplitude noise density at the output of the lock-in amplifier is given by

$$N_A(f) = 2N(f) = \sqrt{2N_{d_{A_F}}(f)^2 + 2N_{e_F}(f)^2} \tag{33}$$

which is obtained by calculating the amplitude probability density function (PDF) and relating the autocorrelation function with that of the in-phase and quadrature states (for details see B). The simulated amplitude noise density function and the linear approximation (33) are shown in Fig. 5(b) for varying cantilever driving amplitudes. The linear model accurately predicts the amplitude noise density in the presence of varying active driving forces, that is for $A_d \neq 0$. However, in contrast to the in-phase noise density in Fig. 5(a), the amplitude noise density is not accurately predicted by the linear model in the absence of an active driving force, that is for $A_d = 0$. In this case, the non-linearities result in a noise whitening effect visible at lower and higher frequencies [31] as highlighted in Fig. 5(b). As is demonstrated in B, since the in-phase and quadrature states are Gaussian distributed [32], the amplitude PDF is a Rician distribution. As can be seen in Fig. 5(c), for $A_d \neq 0$, the amplitude PDF can be approximated by a Gaussian distribution which allows the derivation of the amplitude noise density function $N_A(f) = 2N(f)$ in B. However, this conclusion is not possible for $A_d = 0$ for which the Rician distribution is significantly different to a Gaussian distribution as can be seen in Fig. 5(d).

3.7. *Limit of linear approximation*

It can be noticed in Fig. 5(b), that for purely thermally driven AFM cantilevers subject to electronic noise, the linear approximation (33) does not hold. In other words, the lock-in amplifier becomes an incorrect estimator when the driving amplitude is small compared to the thermal and additive sensor noise.

In Fig. 6(a), a simulation of the lock-in amplifier amplitude noise density estimate for different amplitudes is shown together with the linear approximation (33). It can be seen that for amplitudes smaller than $A \approx 60$ pm, (33) does not hold. Additionally, the total integrated noise

$$\sigma_A = \sqrt{\int_0^{\infty} N_A^2(f)df} \tag{34}$$

shown in Fig. 6(b) and mean of the amplitude shown in Fig. 6(c) are evaluated. To view the accuracy of the lock-in amplifier in estimating of the underlying noise processes, the x-axes in Fig. 6(b) and (c) are scaled by

$$\sigma_e = N_e\sqrt{f_e} \tag{35}$$

where $f_e = \kappa f_{\text{LIA}}$ is the equivalent noise bandwidth which can be readily obtained from the lock-in amplifier low-pass filter cut-off frequency f_{LIA} and κ is a correction factor based on the filter order [33]. If the ratio $A/\sigma_e \gg 1$ (compare the vertical line in Fig. 6(b) and (c)), the signal amplitude is significantly larger than the noise and the lock-in amplifier provides a correct estimate of the amplitude and underlying noise processes. For the noise processes assumed in this simulation and a lock-in amplifier low-pass filter bandwidth of 10 kHz, the minimum amplitude for which a correct estimate is achieved is $A \approx 60$ pm. By lowering the low-pass filter bandwidth to 1 Hz, this limit is improved to $A \approx 100$ fm.

As demonstrated in Section 3.5, the in-phase and quadrature noise spectral density is correct even if $A_d = 0$ unlike the amplitude noise spectral density. As a result, if a lock-in amplifier is used to measure the thermal noise of a cantilever, the in-phase and quadrature noise spectral density should be used instead of the amplitude and the resulting spectrum should be multiplied by 2.

4. Experimental results

In this section, the thermal and amplitude noise spectral densities of three different cantilevers are measured with the OBD sensor of an NT-MDT NTEGRA AFM and compared to the theoretical model derived in the previous section. For this purpose, a high-speed digitizer (Spectrum Netbox DN2.593-08) was used to record 10^9 samples of time-domain cantilever deflection data sampled at 10 MHz. Since both the internal NT-MDT lock-in amplifier and an external lock-in amplifier (Zurich Instruments HF2LI) are limited in output sample rate, the lock-in amplifier configuration shown in Fig. 2 was implemented digitally and the amplitude spectrum was obtained in post-processing. In this way, the amplitude spectral density can be obtained over a wide bandwidth and compared to the proposed LTI model.

In order to clearly highlight the different roll-offs in the amplitude noise spectral density, the demodulation filter bandwidth is set to 10 kHz. If AFM imaging speed is to be optimized, the filter bandwidth should be significantly higher than the cantilever tracking bandwidth and the filter order should be low to increase the phase margin and therefore allow for a higher z-axis controller gain. On the contrary, if low noise AFM imaging is to be performed, the LIA filter bandwidth should be reduced and a higher order can be chosen to minimize the effect of thermal and electronic noise.

Experimental verification of the proposed linear time-invariant model of the amplitude noise spectral density is obtained by measuring three different cantilevers and comparing the direct thermal noise spectrum and the demodulated amplitude noise spectrum. For this reason, cantilevers for very soft tapping mode (NSC19/ALBS) to hard tapping mode (NSC15AlBS) and spanning a wide range of properties with different reflective coating, geometrical properties, Q factors, and stiffnesses are chosen. The parameters of the investigated cantilevers are stated in Table 1. The parameters are obtained from a Lorentzian function fit to the thermal noise response measured with a calibrated Polytec MSA-100 3D laser Doppler vibrometer [23,34] (not shown). Having identified the cantilever stiffness, the Lorentzian function fits to the thermal noise response obtained from the AFM OBD sensors can now be referenced against the MSA measurement to yield the optical lever sensitivities for each cantilever. This calibration approach avoids the necessity to perform amplitude vs. distance approach curves using the AFM.

Table 1
Parameters of cantilevers.

Cantilever	Parameter	Value
NSC15AlBS	f_0	311.1 kHz
	Q	606.0
	k	57.47 N/m
	Ψ_{OBD}	14.4 nm/V
	A	1.62 nm
TAP190G	f_0	156.8 kHz
	Q	522.7
	k	47.65 N/m
	Ψ_{OBD}	20.5 nm/V
	A	4.26 nm
NSC19AlBS	f_0	77.89 kHz
	Q	109.1
	k	0.998 N/m
	Ψ_{OBD}	21.8 nm/V
	A	0.34 nm

4.1. Direct cantilever thermal noise spectra

The direct thermal noise spectra of the three cantilevers measured with the OBD sensor are shown in the first column of Fig. 7. The measured thermal noise spectra are described by

$$N_y(f) = \sqrt{\Psi_{\text{OBD}}^2 N_v(f)^2 + N_d(f)^2} \tag{36}$$

where $N_v(f)$ is the sensor noise spectral density in V/$\sqrt{\text{Hz}}$ and Ψ_{OBD} the optical lever sensitivity of the OBD sensors in m/V. The measurements are compared against the theoretical thermal noise response described by (19). Due to slight differences in the cantilever reflective backside coating, geometrical properties of the cantilever and slightly varying cantilever orientations after alignment, the optical lever sensitivities vary between cantilevers. This highlights the fact that such calibrations need to be performed individually for each cantilever. From the response, the electrical noise floor and thermal noise at resonance can be found. As predicted by (20) and confirmed by the measurements, a low stiffness leads to a high thermal noise at resonance.

4.2. Demodulated amplitude noise spectra

The amplitude noise spectra measured with the OBD sensor of the three cantilevers for an amplitude corresponding to a 10 mV drive (stated in Table 1) and with thermal excitation are shown in the second column of Fig. 7. The low-pass filters employed in the lock-in amplifier are fourth-order RC-filters with a cut-off frequency of 10 kHz. It can be observed that the theoretical spectrum (33) predicts the response for the active drive accurately. From the response, a number of key properties of the cantilever system and instrumentation can be derived. At low frequencies, the noise floor is given by thermal noise at resonance $\sqrt{2}N_d(f_0)$. For increasing frequency, the response rolls off with a corner frequency of $f_c = \frac{f_0}{2Q}$ providing a direct measurement of the cantilever tracking bandwidth. Beyond this corner frequency, the noise floor is

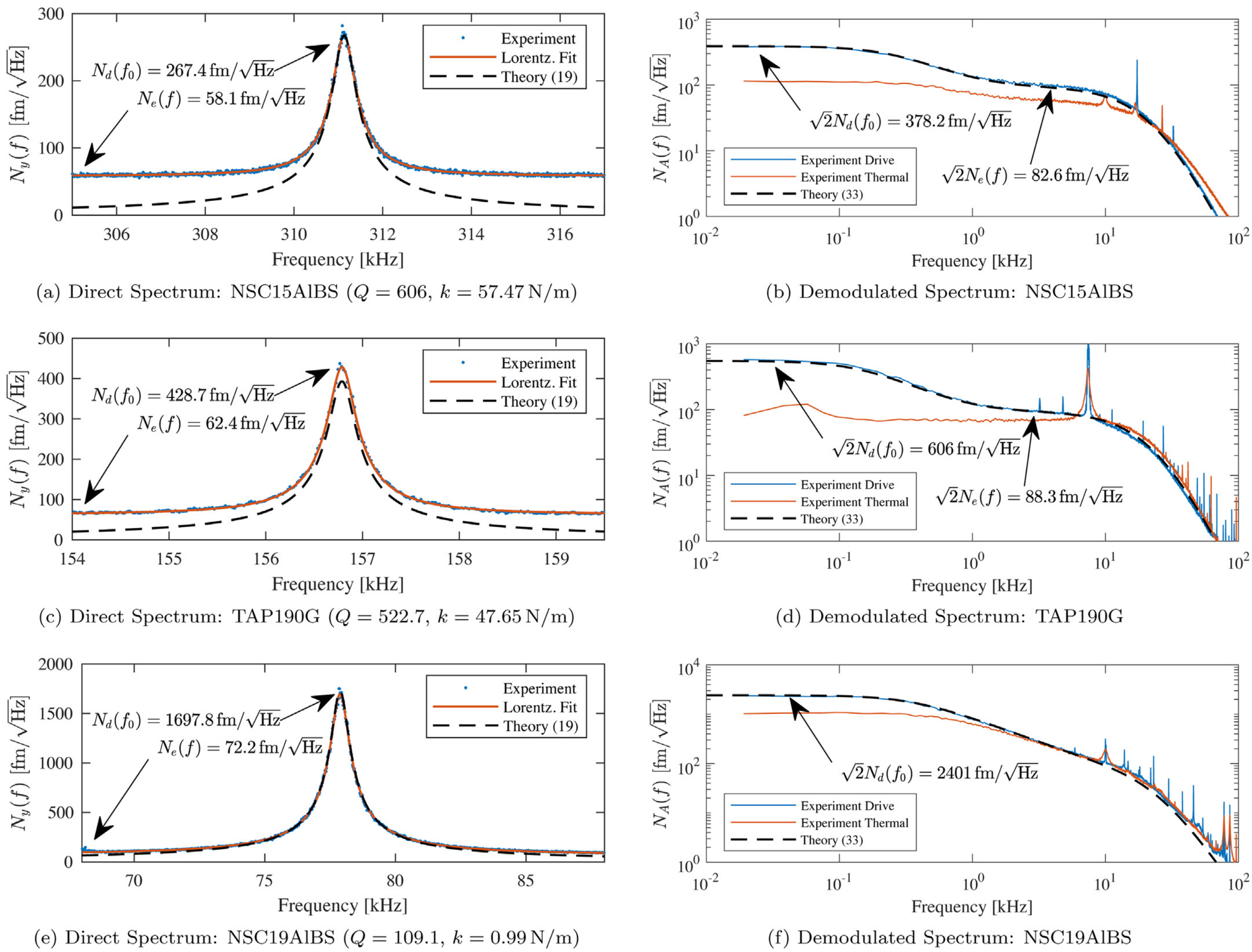

Fig. 7. Experimental verification of the direct cantilever thermal noise density and amplitude noise density using a lock-in amplifier. (a), (c), (e) Direct thermal noise spectra, Lorentzian function fit and theoretical thermal noise response (19) of the three cantilevers stated in Table 1. (b), (d), (f) Demodulated amplitude noise spectra for a direct excitation of 10 mV, thermal excitation and theoretical amplitude noise density (33) of the three cantilevers stated in Table 1.

given by the electrical noise floor of the cantilever instrumentation $\sqrt{2}N_e(f)$. Finally, the response rolls off at the lock-in amplifier low-pass filter cut-off frequency. For thermal excitation only, a noise whitening can be observed as predicted by the simulations in Fig. 5.

5. Conclusions

The lock-in amplifier is an integral part of dynamic imaging modes in atomic force microscopy. The multiplication and low-pass filtering in the implementation affects both the imaging bandwidth and the noise in the amplitude estimate. In this paper, we have performed a detailed analysis of the noise spectra of the cantilever deflection signal due to thermal noise and electronic instrumentation noise as it propagates through the lock-in amplifier. Despite the nonlinearities in the calculation of the oscillation amplitude, the amplitude noise spectral density can be predicted by a linear time-invariant filter response given by the cantilever amplitude dynamics and low-pass filters inside the lock-in amplifier. From this spectrum, important parameters of the cantilever system can be obtained including the thermal noise at resonance, the cantilever tracking bandwidth, and the electronic noise floor of the instrumentation. Compared to conventional ways of obtaining these values, the approach using the amplitude noise spectral density has a lower computational burden on the signal processing system and avoids tip-sample contact for obtaining the cantilever tracking bandwidth. In future work, the authors aim to use the linear time-invariant model for z-axis controller design and to predict the total noise in an AFM image considering the external noise processes.

Credit author statement

Michael Ruppert: Conceptualization, Methodology, Software, Validation, Formal Analysis, Investigation, Writing – Original Draft, Visualization, Project administration.

Nathan Bartlett: Formal Analysis, Writing – Reviewing and Editing.

Yuen Yong: Funding acquisition, Writing – Reviewing and Editing.

Andrew Fleming: Supervision, Writing – Reviewing and Editing.

Appendix A. Proof of in-phase and quadrature noise spectral density

A.1 Multiplying white noise with a sinusoid

Let $n(t)$ denote a stationary white noise process with power spectral density $S_n(f)$, e.g. white sensor noise. Further, let Θ denote a random phase offset. The power spectral density of the process

$$y(t)=n(t)\cos(2\pi f_0 t+\Theta) \tag{A.1}$$

is given by [32,Equation (1.55)]

$$S_y(f)=\frac{1}{4}\left[S_n(f-f_0)+S_n(f+f_0)\right]=\frac{1}{2}S_n(f). \tag{A.2}$$

Taking the square-root of the power spectral density yields

$$N_y(f)=\frac{\sqrt{2}}{2}N_n(f) \tag{A.3}$$

which yields the pre-factor for $N_{e,F}(f)$ in (31).

A.2 Multiplying narrowband noise with a sinusoid

Let $n(t)$ denote a narrow band noise process of bandwidth $2f_b$ centered at the frequency f_0 with power spectral density $S_n(f)$, e.g. thermal force noise exciting the cantilever resonance. The power spectral densities of $y_i(t)=n(t)2\sin(2\pi f_0 t)$ and $y_q(t)=n(t)2\cos(2\pi f_0 t)$ for $-f_b\le f\le f_b$ are given by [32,Equation (1.101)]

$$\begin{aligned} S_{y_i}(f) &= S_n(f-f_0)+S_n(f+f_0)=2S_n(f)\\ S_{y_q}(f) &= S_n(f-f_0)+S_n(f+f_0)=2S_n(f)\end{aligned} \tag{A.4}$$

which implies

$$S_{\frac{1}{2}y_i}(f)=S_{\frac{1}{2}y_q}(f)=\frac{1}{2}S_n(f). \tag{A.5}$$

Taking the square-root of the power spectral density yields

$$N_{\frac{1}{2}y_i}(f)=N_{\frac{1}{2}y_q}(f)=\frac{\sqrt{2}}{2}N_n(f) \tag{A.6}$$

which yields the pre-factor for $N_{d_A,F}(f)$ in (31).

Appendix B. Proof of amplitude noise density

B.1 General

Let X denote a random variable. Using [33,Equation 1.8.10] and [35,Equation (9-163)], the noise spectral density $N_X(f)$ and variance σ_X^2 are related by

$$\sigma_X^2+\mathbb{E}[X]^2=\mathbb{E}[X^2]=\int_0^\infty N_X(f)^2 df. \tag{B.1}$$

Define the centered random variable $\overline{X}=X-\mathbb{E}[X]$ [35,Equation (9-70)] such that the mean $\mathbb{E}[\overline{X}]=0$ and the variance $\sigma_{\overline{X}}^2=\sigma_X^2$. Using (B.1), the variance can be determined from the integral over the noise spectral density $N_{\overline{X}}(f)$

$$\sigma_{\overline{X}}^2=\int_0^\infty N_{\overline{X}}(f)^2 df. \tag{B.2}$$

B.2 Amplitude probability density function

Consider a signal $y(t)$ with angular frequency ω_0, random amplitude A and random phase ϕ as per (1)

$$y(t)=A\sin(\omega_0 t+\phi)\,. \tag{B.3}$$

The amplitude is given by the in-phase and quadrature states

$$x_i=A\cos\phi \tag{B.4a}$$

$$x_q=A\sin\phi \tag{B.4b}$$

and can be obtained by (5), or equivalently

$$A=\sqrt{x_i^2+x_q^2}. \tag{B.5}$$

In order to obtain the probability density function $p(A)$ and centered noise spectral density $N_A(f)$ of the amplitude A, it is assumed that the in-phase state x_i and quadrature state x_q are normally (Gaussian) distributed with respective means μ_i, μ_q and equal variance σ^2 [32], that is

$$x_i\sim\mathcal{N}(\mu_i,\,\sigma^2) \tag{B.6a}$$

$$x_q\sim\mathcal{N}(\mu_q,\,\sigma^2). \tag{B.6b}$$

with means

$$\mu_i=\mathbb{E}[x_i]=A_d\cos\phi \tag{B.7a}$$

$$\mu_q=\mathbb{E}\left[x_q\right]=A_d\sin\phi \tag{B.7b}$$

and A_d is the expected amplitude as defined in (11) in the absence of noise. The probability density functions are given by

$$p(x_i)=\frac{1}{\sigma\sqrt{2\pi}}e^{-\frac{1}{2}\left(\frac{x_i-A_d\cos\phi}{\sigma}\right)^2}, \tag{B.8a}$$

$$p(x_q)=\frac{1}{\sigma\sqrt{2\pi}}e^{-\frac{1}{2}\left(\frac{x_q-A_d\sin\phi}{\sigma}\right)^2}. \tag{B.8b}$$

Now consider the centered in-phase and quadrature states [35] such that their respective means are zero

$$\overline{x}_i=x_i-\mathbb{E}[x_i] \tag{B.9a}$$

$$\overline{x}_q=x_q-\mathbb{E}\left[x_q\right]. \tag{B.9b}$$

Then, it holds that

$$\sigma^2=\mathbb{E}\left[(\overline{x}_i)^2\right]=\mathbb{E}\left[\left(\overline{x}_q\right)^2\right]=\int_0^\infty(2N)^2(f)df. \tag{B.10a}$$

Define $z_i=x_i^2$ and $z_q=x_q^2$. From [36,Theorem 3.5.1] z_i and z_q are statistically independent non-central Wishart random variables with the following distributions:

$$p(z_i)=\frac{1}{\sigma\sqrt{2\pi z_i}}e^{-\left(\frac{z_i+A_d^2\cos\phi^2}{2\sigma^2}\right)}{}_0F_1\left(\frac{1}{2};\frac{A_d^2\cos\phi^2 z_i}{4\sigma^4}\right), \tag{B.11a}$$

$$p(z_q)=\frac{1}{\sigma\sqrt{2\pi z_q}}e^{-\left(\frac{z_q+A_d^2\sin\phi^2}{2\sigma^2}\right)}{}_0F_1\left(\frac{1}{2};\frac{A_d^2\sin\phi^2 z_q}{4\sigma^4}\right), \tag{B.11b}$$

where ${}_0F_1(\cdot)$ denotes the confluent hypergeometric function. Let $w=z_i+z_q$, using [36,Theorem 3.5.5], the summed squared in-phase and quadrature states are also non-central Wishart distributed as

$$p(w)=\frac{1}{2\sigma^2}e^{-\frac{1}{2}\left(\frac{w+A_d^2}{\sigma^2}\right)}I_0\left(\frac{\sqrt{w}A_d}{\sigma^2}\right), \tag{B.12}$$

where $I_0(\cdot)$ is the zeroth-order modified Bessel function of the first kind [37]. Finally, in order to satisfy (B.5), let $A=\sqrt{w}$, then using [36,Equation 1.3.14], the probability density function of A is equal to

$$p(A)=\frac{A}{\sigma^2}e^{-\frac{1}{2}\left(\frac{A^2+A_d^2}{\sigma^2}\right)}I_0\left(\frac{AA_d}{\sigma^2}\right), \tag{B.13}$$

which corresponds to a Rician distribution $\mathcal{R}(A|\nu,\,\rho)$ with spread $\rho=\sigma$ and distance $\nu=A_d$ [38].

B.3 Amplitude noise spectral density

With the definition of the centered random variables (B.9a), (B.9b) and $\overline{A} = A - \mathbb{E}[A]$, taking the square of(5), and substituting the above centered random variables yields the following equality:

$$\left(\overline{A} + \mathbb{E}[A]\right)^2 = (\bar{x}_i + A_d \cos\phi)^2 + \left(\bar{x}_q + A_d \sin\phi\right)^2. \tag{B.14}$$

Let $A_d \gg \sigma$, then the probability density function (B.13) can be approximated by a Gaussian distribution with $\mathbb{E}[A] = A_d$ and variance σ^2 (compare [32] and Fig. 5). Substituting this approximation into (B.14) and re-arranging,

$$\sigma\overline{A} = \frac{\sigma}{2A_d}(\bar{x}_i^2 + \bar{x}_q^2 - \overline{A}^2) + \sigma(\bar{x}_i \cos\phi + \bar{x}_q \sin\phi), \tag{B.15}$$

Because $A_d \gg \sigma$, the first term on the right hand side is significantly smaller than all other terms. Therefore, we assume this term is negligible, and obtain the approximate solution

$$\overline{A} = \bar{x}_i \cos\phi + \bar{x}_q \sin\phi. \tag{B.16}$$

We now have the centered amplitude in terms of the centered in-phase and quadrature states, enabling us to obtain the auto-correlation of A:

$$\begin{aligned} R_A(\tau) &= \mathbb{E}[\overline{A}(t)\overline{A}(t+\tau)], \\ &= R_{x_i}(\tau)\cos^2\phi + R_{x_q}(\tau)\sin^2\phi. \end{aligned} \tag{B.17}$$

By definition [35,Equation (9-133)], the noise spectral densities of x_i, x_q and A are given by

$$N_A^2(f) = \int_{-\infty}^{\infty} R_A(\tau) e^{-j2\pi f\tau} d\tau, \tag{B.18a}$$

$$N_{x_i}^2(f) = \int_{-\infty}^{\infty} R_{x_i}(\tau) e^{-j2\pi f\tau} d\tau, \tag{B.18b}$$

$$N_{x_q}^2(f) = \int_{-\infty}^{\infty} R_{x_q}(\tau) e^{-j2\pi f\tau} d\tau. \tag{B.18c}$$

Substituting (B.17) in (B.18a) yields

$$\begin{aligned} N_A^2(f) &= \cos^2\phi \int_{-\infty}^{\infty} R_{x_i}(\tau) e^{-j2\pi f\tau} d\tau \\ &+ \sin^2\phi \int_{-\infty}^{\infty} R_{x_q}(\tau) e^{-j2\pi f\tau} d\tau \end{aligned} \tag{B.19}$$

which, using (B.18b) and (B.18c) is equivalent to

$$N_A^2(f) = \cos^2\phi N_{x_i}^2(f) + \sin^2\phi N_{x_q}^2(f). \tag{B.20}$$

Since $N_{x_i}(f) = N_{x_q}(f) \triangleq 2N(f)$, the noise spectral density of A is equal to:

$$\begin{aligned} N_A^2(f) &= (2N(f))^2(\cos^2\phi + \sin^2\phi), \\ &= (2N(f))^2. \end{aligned} \tag{B.21}$$

Taking the square root of (B.21) yields

$$N_A(f) = 2N(f). \tag{B.22}$$

We remark that the above result is an approximation, and will only be accurate if $A_d \gg \sigma$. Thus, this result cannot be utilized if $A_d = 0$.

References

[1] A.J. Fleming, A review of nanometer resolution position sensors: operation and performance, Sens. Actuators A 190 (2013) 106–126, http://dx.doi.org/10.1016/j.sna.2012.10.016.

[2] D.S. Nyce, Linear Position Sensors: Theory and Application, John Wiley & Sons, 2004.

[3] L.K. Baxter, Capacitive sensors: design and applications, Ann Arbor 1001 (2000) 48109.

[4] S.D. Roach, Designing and building an eddy current position sensor, Sens. J. Appl. Sens. Technol. 15 (9) (1998) 56–74.

[5] R. García, R. Perez, Dynamic atomic force microscopy methods, Surf. Sci. Rep. 47 (6–8) (2002) 197–301, http://dx.doi.org/10.1016/S0167-5729(02)00077-8.

[6] G. Binnig, C.F. Quate, C. Gerber, Atomic force microscope, Phys. Rev. Lett. 56 (1986) 930–933, http://dx.doi.org/10.1103/PhysRevLett.56.930.

[7] L. Gross, F. Mohn, N. Moll, P. Liljeroth, G. Meyer, The chemical structure of a molecule resolved by atomic force microscopy, Science 325 (5944) (2009) 1110–1114.

[8] E.T. Herruzo, A.P. Perrino, R. Garcia, Fast nanomechanical spectroscopy of soft matter, Nat. Commun. 5 (3126) (2014) 1–8.

[9] T. Ando, N. Kodera, E. Takai, D. Maruyama, K. Saito, A. Toda, A high-speed atomic force microscope for studying biological macromolecules, Proc. Natl. Acad. Sci. 98 (22) (2001) 12468–12472, http://dx.doi.org/10.1073/pnas.211400898.

[10] D. Abramovitch, Low latency demodulation for atomic force microscopes, Part I Efficient real-time integration, American Control Conference (2011) 2252–2257, http://dx.doi.org/10.1109/ACC.2011.5991144.

[11] M.G. Ruppert, K.S. Karvinen, S.L. Wiggins, S.O. Reza Moheimani, A Kalman filter for amplitude estimation in high-speed dynamic mode atomic force microscopy, IEEE Trans. Control Syst. Technol. 24 (1) (2016) 276–284, http://dx.doi.org/10.1109/TCST.2015.2435654.

[12] M.R.P. Ragazzon, M.G. Ruppert, D.M. Harcombe, A.J. Fleming, J.T. Gravdahl, Lyapunov estimator for high-speed demodulation in dynamic mode atomic force microscopy, IEEE Trans. Control Syst. Technol. 26 (2) (2017) 765–772, http://dx.doi.org/10.1109/TCST.2017.2692721.

[13] D. Platz, E.A. Tholén, D. Pesen, D.B. Haviland, Intermodulation atomic force microscopy, Appl. Phys. Lett. 92 (15) (2008) 153106, http://dx.doi.org/10.1063/1.2909569.

[14] M.G. Ruppert, D.M. Harcombe, S.O.R. Moheimani, High-bandwidth demodulation in MF-AFM: a Kalman filtering approach, IEEE/ASME Trans. Mechatron. 21 (6) (2016) 2705–2715, http://dx.doi.org/10.1109/TMECH.2016.2574640.

[15] D.M. Harcombe, M.G. Ruppert, M.R.P. Ragazzon, A.J. Fleming, Lyapunov estimation for high-speed demodulation in multifrequency atomic force microscopy, Beilstein J. Nanotechnol. 9 (2018) 490–498, http://dx.doi.org/10.3762/bjnano.9.47.

[16] M.G. Ruppert, D.M. Harcombe, M.R.P. Ragazzon, S.O.R. Moheimani, A.J. Fleming, A review of demodulation techniques for amplitude-modulation atomic force microscopy, Beilstein J. Nanotechnol. 8 (2017) 1407–1426, http://dx.doi.org/10.3762/bjnano.8.142.

[17] C.R. Cosens, A balance-detector for alternating-current bridges, Proc. Phys. Soc. 46 (6) (1934) 818.

[18] W.C. Michels, N.L. Curtis, A pentode lock-in amplifier of high frequency selectivity, Rev. Sci. Instrum. 12 (9) (1941) 444–447, http://dx.doi.org/10.1063/1.1769919.

[19] E.D. Morris, H.S. Johnston, Digital phase sensitive detector, Rev. Sci. Instrum. 39 (4) (1968) 620–621, http://dx.doi.org/10.1063/1.1683462.

[20] M. Carminati, G. Ferrari, M. Sampietro, Attofarad resolution potentiostat for electrochemical measurements on nanoscale biomolecular interfacial systems, Rev. Sci. Instrum. 80 (12) (2009) 124701, http://dx.doi.org/10.1063/1.3245343.

[21] G. Gervasoni, M. Carminati, G. Ferrari, Switched ratiometric lock-in amplifier enabling sub-ppm measurements in a wide frequency range, Rev. Sci. Instrum. 88 (10) (2017) 104704, http://dx.doi.org/10.1063/1.4996423.

[22] G. Meyer, N.M. Amer, Novel optical approach to atomic force microscopy, Appl. Phys. Lett. 53 (12) (1988) 1045–1047, http://dx.doi.org/10.1063/1.100061.

[23] J.L. Hutter, J. Bechhoefer, Calibration of atomic force microscope tips, Rev. Sci. Instrum. 64 (7) (1993) 1868–1873, http://dx.doi.org/10.1063/1.1143970.

[24] H.J. Butt, M. Jaschke, Calculation of thermal noise in atomic force tapping-mode, Nanotechnology 6 (1) (1995) 1.

[25] E. Alexander, D. Poularikas, The Handbook of Formulas and Tables for Signal Processing, 73, 1998.

[26] T. Fukuma, M. Kimura, K. Kobayashi, K. Matsushige, H. Yamada, Development of low noise cantilever deflection sensor for multienvironment frequency-modulation atomic force microscopy, Rev. Sci. Instrum. 76 (5) (2005), http://dx.doi.org/10.1063/1.1896938.

[27] T. Fukuma, Wideband low-noise optical beam deflection sensor with photothermal excitation for liquid-environment atomic force microscopy, Rev. Sci. Instrum. 80 (2) (2009) 023707, http://dx.doi.org/10.1063/1.3086418.

[28] M. Dukic, J.D. Adams, G.E. Fantner, Piezoresistive AFM cantilevers surpassing standard optical beam deflection in low noise topography imaging, Sci. Rep. 5 (16393) (2015) 1–11, http://dx.doi.org/10.1038/srep16393.

[29] J. Kokavecz, Z.L. Horváth, Á. Mechler, Dynamical properties of the Q-controlled atomic force microscope, Appl. Phys. Lett. 85 (15) (2004) 3232–3234, http://dx.doi.org/10.1063/1.1785863.

[30] L. Chen, X. Yu, D. Wang, Cantilever dynamics and quality factor control in AC mode AFM height measurements, Ultramicroscopy 107 (4-5) (2007) 275–280, http://dx.doi.org/10.1016/j.ultramic.2006.06.006.

[31] G. Wise, A. Traganitis, J. Thomas, The effect of a memoryless nonlinearity on the spectrum of a random process, IEEE Trans. Inf. Theory 23 (1) (1977) 84–89.

[32] S. Haykin, Communication Systems, John Wiley & Sons, 2008.

[33] R.G. Brown, P.Y.C. Hwang, Introduction to Random Signals and Applied Kalman Filtering, John Wiley & Sons Inc., 1997.

[34] J.E. Sader, J.A. Sanelli, B.D. Adamson, J.P. Monty, X. Wei, S.A. Crawford, J.R. Friend, I. Marusic, P. Mulvaney, E.J. Bieske, Spring constant calibration of atomic force microscope cantilevers of arbitrary shape, Rev. Sci. Instrum. 83 (10) (2012) 103705, http://dx.doi.org/10.1063/1.4757398.
[35] A. Papoulis, S.U. Pillai, Probability, Random Variables, and Stochastic Processes, Tata McGraw-Hill Education, 2002.
[36] A. Gupta, D. Nagar, Matrix Variate Distributions. Monographs and Surveys in Pure and Applied Mathematics, Chapman & Hall/CRC, London, 2000.
[37] G.N. Watson, A Treatise on the Theory of Bessel Functions, Cambridge University Press, 1995.
[38] J. Sijbers, A.J. den Dekker, P. Scheunders, D. Van Dyck, Maximum-likelihood estimation of rician distribution parameters, IEEE Trans. Med. Imaging 17 (3) (1998) 357–361.

Biographies

Michael G. Ruppert received the Dipl.-Ing. degree in automation technology from the University of Stuttgart, Germany, in 2013 and the PhD degree in Electrical Engineering from The University of Newcastle, Australia in 2017. As a visiting researcher, he was with The University of Texas at Dallas, USA from 2015 until 2016 and he is currently a postdoctoral research fellow at The University of Newcastle. His research interests include the utilization of system theoretic tools for sensing, estimation and control in high-speed and multifrequency atomic force microscopy. Dr. Ruppert's research has been recognized with the 2019 Best Conference Paper Award at the 2019 International Conference on Manipulation, Automation and Robotics at Small Scales (MARSS), the 2018 IEEE Transactions on Control Systems Technology Outstanding Paper Award, and the 2017 University of Newcastle Higher Degree by Research Excellence Award.

Nathan J. Bartlett received his B.E. (Mechatronics) with first-class honours from The University of Newcastle, Australia, (Callaghan Campus) in May 2015. Between 2015 and 2019, he was the CTO of a deep-tech startup. At present, he is working toward a Ph.D. degree at The University of Newcastle. The focus of his research includes Bayesian probability, random variable transformations, sensor fusion, and extended target tracking.

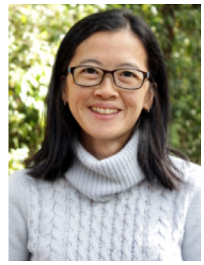

Yuen K. Yong received the Bachelor of Engineering degree in Mechatronics Engineering and the PhD degree in Mechanical Engineering from The University of Adelaide, Australia, in 2001 and 2007, respectively. She is current an associate professor at The University of Newcastle, Australia. Her research interests include nanopositioning systems, design and control of microcantilevers, atomic force microscopy, and miniature robotics. Dr. Yong was an Australian Research Council DECRA fellow from 2013 to 2017. She is an associate editor for the IEEE/ASME Transactions of Mechatronics. She was the recipient of the University of Newcastle Vice-Chancellor's Award for Research Excellence in 2014 and the Vice-Chancellor's Award for Research Supervision Excellence in 2017.

fx5**Andrew J. Fleming** (M'02) received the B.Sc. degree in electrical engineering and the Ph.D. degree in mechatronics engineering from the University of Newcastle, Callaghan, NSW, Australia, in 2000 and 2004, respectively. He is currently an Australian Research Council Future Fellow and the Director with the Precision Mechatronics Lab, University of Newcastle. He is the co-author of three books, and more than 180 journal and conference articles. He is the Inventor of several patent applications. His research interests include lithography, nanopositioning, scanning probe microscopy, and biomedical devices. Dr. Fleming received the Academy for Technological Sciences and Engineering Baterham Medal in 2016, the Newcastle Innovation Rising Star Award for Excellence in Industrial Engagement in 2012, the IEEE Control Systems Society Outstanding Paper Award in 2007, and the University of Newcastle Researcher of the Year Award in 2007.